Journal of Sound and Vibration (2002) **253**(5), 961–983
doi:10.1006/jsvi.2001.3945, available online at http://www.idealibrary.com on IDEAL®

RADIAL FORCE TRANSMISSION TO THE HUB FROM AN UNLOADED STATIONARY TYRE

R. J. PINNINGTON

Institute of Sound and Vibration Research, University of Southampton, Highfield Southampton, SO17 1BJ, England. E-mail: rjp@soton.ac.uk

(*Received* 12 *May* 1999, *and in final form* 21 *June* 2001)

The static and dynamic stiffness of a tyre sidewall are calculated as a function of geometry, load parameters and frequency. Two different expressions were used for below and above the ring frequency. The air pressure and section aspect ratio are found to be the controlling influences below the ring frequency. This sidewall stiffness was inserted into previously obtained wave equations to obtain the dispersion relationships and impedances for a tyre belt with sidewalls. The stiffness and force transmission to the hub in the region of the contact patch was also calculated and compared with measured values. The sidewall stiffness in the region of the contact patch is found to be strongly dependent on the belt wavespeed, giving a stiffer value in the region of the contact patch above the ring frequency.

1. INTRODUCTION

Some wave equations for a tyre belt were presented in reference [1]. These included the effects of bending, shear tension, rotary inertia and also an arbitrary edge impedance to describe the sidewall. These were used to make wavespeed, mobility and attenuation predictions suitable for high-frequency calculations of sound radiation. The effect of the sidewall was not included as it required an independent study and also for conventional geometry it is not very influential with regard to propagation of vibration on the belt above the belt-sidewall natural frequency which occurs around 100 Hz.

The main purpose of the sidewall is to transmit traction and also steering moments from the hub to the belt. It will also influence the belt vibration and be responsible for transmitting dynamic forces to the hub that lead to interior vehicle noise. The objective here then is to study both of these effects.

The sidewall is usually regarded as either a simple spring, or springs in the tangential and radial directions [2–6]. The spring stiffness is identified by experimental modal analysis or by finite element calculations, which seem to be adequate for practical purposes until about 300 Hz [4]. A more physical model is presented here in two parts: below the ring frequency (about 300 Hz) of the sidewall there is a "static" model of a pressurized inextensible curved membrane under tension; above the ring frequency, there is a "dynamic model" of a beam transmitting tension, bending and compression waves. The problem is divided in this manner about the ring frequency to simplify the analysis.

At low frequencies in the regime of the "static" model the sidewall and enclosed air transmit forces to the hub in two modes. The first regards the sidewall as inextensible, when radially inward motion of the belt is accompanied by sidewall bulging which conserves the enclosed air volume and causes no coupling to the toroidal acoustic space. The second is the

0022-460X/02/$35.00

breathing mode of the tyre section, involving stretching of the sidewall and consequent coupling with the air space within [7, 8]. The sidewall is much softer in the first mechanism described and so this tends to dominate over most of the frequency range. The second mechanism is thought to be only important for the excitation of the tyre acoustic cavity mode at about 250 Hz for saloon vehicles, when the cavity circumference is equal to an acoustic wavelength. Only the first mechanism, where the sidewall is inextensible, is considered here in the "static" model.

The static stiffness is calculated as a function of internal pressure, external load, bending stiffness, and the angle subtended by the sidewall. The sidewall stiffness is found to be strongly non-linear on account of high sensitivity to this last parameter. The angle subtended to the sidewall is a function of both the load and the tyre section aspect ratio.

A dynamic model is also proposed for the region above the sidewall section ring frequency when the curvature may be neglected. Bending, compression and tension waves are included to calculate the input and transfer dynamic stiffnesses relevant to the connection at the belt and the force transmission to the hub. The wavelength of the input line displacement is found to be very important, giving very different dynamic stiffnesses in the region of the belt and contact patch.

The sidewall model presented is not accurate between about 200 Hz on a car tyre and the ring frequency of the sidewall around 500 Hz. In practice, bending waves can also propagate in this region, but these waves are not included here in this frequency region. This omission will have little influence on the coupled belt dynamics but calculations of transmitted force to the hub in this frequency region will not be correct.

The sidewall model is coupled with the belt wave model to make input mobility predictions and belt attenuation predictions on a point loaded infinite belt with a sidewall. Measurements of input and transfer characteristics around the belt and to the hub were made on a tyre at various pressures, and the results compared with predictions [3].

2. THE SIDEWALL MODEL BELOW THE RING FREQUENCY

The sidewall links the belt to the hub and contributes a line impedance Z_S/length, in reference [1] equation (10), to the belt dynamics. The sidewall is also responsible for most of the force transmission to the hub. The main features are that it is a curved structure and also that it transmits forces by tension, bending and axial force. The input stiffness/length at the belt K_S and the transfer stiffness/length, K_T, from the belt to the hub are calculated.

At frequencies below the ring frequency of the sidewall (typically 200–400 Hz) the sidewall assumes two possible deformation patterns, these are shown in Figure 1.

Case (a) shows the deformation when the sidewall is inextensible. The air volume is conserved and these sidewall motions do not couple into the cavity acoustic modes.

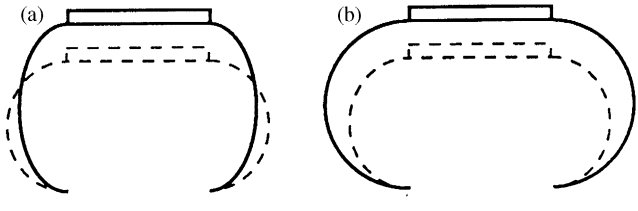

Figure 1. Cross-sectional deformation patterns of (a) bending, (b) stretching.

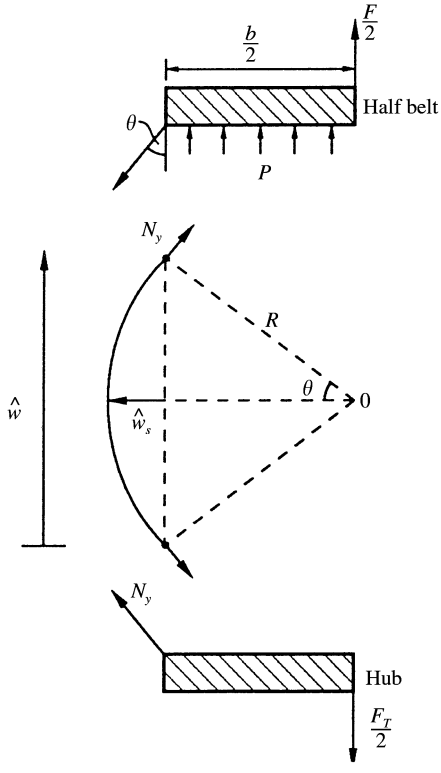

Figure 2. Forces on half tyre section.

Case (b), not considered here, shows the deformation due to sidewall stretching. This wave type couples into the air space. For measurements taken of sidewall deformation [3] only case (a) was observed as being associated with belt motion below 300 Hz.

Consider the half cross-section in Figure 2 where an external force F acts over the width of the belt. The sidewall is assumed to take a circular section, as this is the form taken by a pressurized membrane. The sidewall, subjected to tension N_y, is inextensible of length l_s, taking a radius $R = l_s/2\theta$. Vertical equilibrum of the belt yields

$$F = 2N_y \cos\theta - Pb + m_s\ddot{w}, \tag{1}$$

where P is the pressure. The horizontal equilibrium of the sidewall gives

$$2\sin\theta(PR - N_y) = m_s\ddot{w}_s, \tag{2}$$

where m_s is the modal mass (approximately the mass/2).

The total height of the sidewall $\hat{w}$ is

$$\hat{w} = \frac{l_s \sin\theta}{\theta} \tag{3}$$

while the sidewall lateral displacement $\hat{w}_s$ is

$$\hat{w}_s = \frac{l_s(1 - \cos\theta)}{2\theta}. \tag{4}$$

For small displacements w and w_s at any angle θ become

$$w = \frac{\mathrm{d}\hat{w}}{\mathrm{d}\theta}\,\delta\theta, \qquad w_s = \frac{\mathrm{d}\hat{w}_s}{\mathrm{d}\theta}\,\delta\theta \tag{5}$$

which from equations (3) and (4) give the ratio

$$\frac{w_s}{w} = \frac{\theta}{2}\left(\frac{\theta\cos\theta + \sin\theta}{\theta\cos\theta - \sin\theta}\right). \tag{6}$$

For the range of angles under consideration ($0 < \theta < \pi/2$)

$$\sin\theta \approx \theta - \frac{\theta^3}{6}, \cos\theta \approx 1 - \frac{\theta^2}{2} \tag{7}$$

so

$$\frac{w_s}{w} \approx -\frac{3}{\theta} + \theta. \tag{8}$$

This expression has a 6% error around typical equilibrium angles of 45°. At the limit of $\pi/2$ the error is a maximum of 50%. The sidewall tension N_y in equation (2) can likewise be written as

$$N_y \approx \frac{Pl_s}{2\theta} + \frac{m_s\ddot{w}}{2\sin\theta}\left(\frac{3}{\theta} - \theta\right). \tag{9}$$

The input force F and the transmitted force F_T are given from equation (1) as

$$F = F_T = \frac{\cos\theta}{\theta}\left(Pl_s + \frac{3m_s\ddot{w}}{\sin\theta}\left(1 - \frac{\theta^2}{3}\right)\right) - Pb + m_s\ddot{w}. \tag{10}$$

The first bracketted term is the force transmitted by the sidewall, which is a function of angle. The second term, in opposition, is a constant force due to the air pressure. The static force, F, is borne by the air pressure, while the dynamic fluctuations are accommodated by the angle variation of the sidewall.

2.1. STATIC DEFORMATION WITH ZERO EXTERNAL FORCE F

The static force F borne by a section of tyre is shown from equation (10) to be a function of sidewall angle θ, i.e.,

$$F = P\left(\frac{l_s\cos\theta}{\theta} - b\right). \tag{11}$$

The pressure P acts on an effective length shown in the brackets, which is the distance O–O in Figure 3. An increase in the compressive load, $-F$, is accommodated by an increase in θ (and length O–O), until the maximum of $-Pb$ when $\theta = \pi/2$. When the belt is unloaded (away from the contact patch), the equilibrium angle θ_0 is obtained from equation (11), i.e.

$$\frac{\theta_0}{\cos\theta_0} = \frac{l_s}{b}. \tag{12}$$

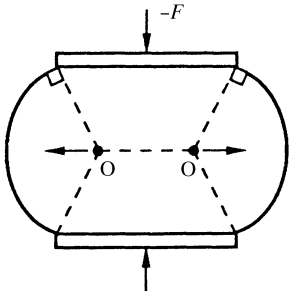

Figure 3. Section of a tyre showing the effective pressure zone.

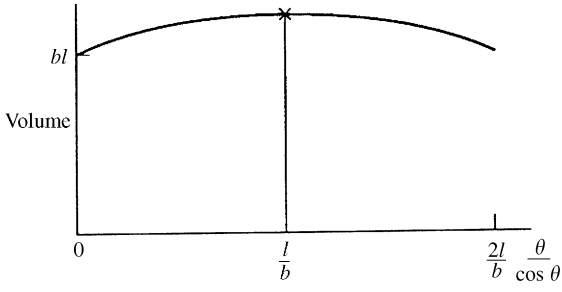

Figure 4. Cavity volume as a function of angle, $\theta/\cos\theta$.

The load distance O–O becomes zero, indicating that the pressure force is balanced by the opposing sidewall tension. The two sidewall arcs then become part of a circle with the same centre. Subsequent dynamic analyses will consider perturbations from this equilibrium angle, which will be appropriate for the wave transmission calculated in the coupled belt and sidewall.

2.2. THE CAVITY VOLUME

The volume V of the cavity/belt length can be calculated from the geometry of Figure 2 as

$$V = bl_s\left(\frac{\sin\theta}{\theta} + \frac{l_s}{b}\left(\frac{1}{2\theta}\right)\left(1 - \frac{\sin 2\theta}{2\theta}\right)\right) \tag{13}$$

which is plotted in Figure 4.

The differential of equation (13)

$$\frac{\mathrm{d}V}{\mathrm{d}\theta} = \frac{bl_s}{\theta^2}(\theta\cos\theta - \sin\theta)\left(1 - \frac{l_s}{b}\frac{\cos\theta}{\theta}\right), \tag{14}$$

gives the maximum volume at the zero slope condition when $\theta/\cos\theta = l_s/b$. This corresponds to the equilibrium angle θ_0 described in equation (12). The important implication of this finding is that small perturbations about the equilibum angle will not be accompanied by changes in volume and hence there will be no coupling at the acoustic space within. Apart from providing the tension within the sidewall the air does not directly influence the transmission of vibration in this mode of behaviour.

2.3. FORCE–DISPLACEMENT RELATIONSHIPS

The static stiffness K_T of one sidewall due to small perturbations w of the belt can be found by differentiating equations (10) and (3) with respect to θ and dividing, i.e.,

$$K_T = \frac{1}{2}\frac{\mathrm{d}F}{\mathrm{d}\theta}\Big/\frac{\mathrm{d}\hat{w}}{\mathrm{d}\theta}, \tag{15}$$

where

$$\frac{1}{2}\frac{\mathrm{d}F}{\mathrm{d}\theta} = -\frac{Pl_s}{2\theta}\left(\sin\theta\frac{\cos\theta}{\theta}\right), \quad \frac{\mathrm{d}\hat{w}}{\mathrm{d}\theta} = \frac{1}{\theta}\left(\cos\theta - \frac{\sin\theta}{\theta}\right) \tag{16}$$

giving

$$K_T = -\frac{P}{2}\left(\frac{\theta\sin\theta + \cos\theta}{\theta\cos\theta - \sin\theta}\right). \tag{17}$$

Using the small angle approximations of equation (7) the stiffness is

$$K_T = \frac{P}{4\theta^3}(6 + 3\theta^2 - \theta^4), \quad 0 < \theta < \pi/2. \tag{18}$$

Equation (17), normalized to the pressure is plotted in Figure 5 as a function of angle.

Also plotted in Figure 5 is the sidewall stiffness or external force F/Pb taken from equation (10), i.e.,

$$\frac{F}{Pb} = \frac{l_s}{b}\frac{\cos\theta}{\theta} - 1. \tag{19}$$

The stiffness is seen to change with the load and so gives a non-linear relationship between the imposed displacement at the road surface and the force transmitted to the hub.

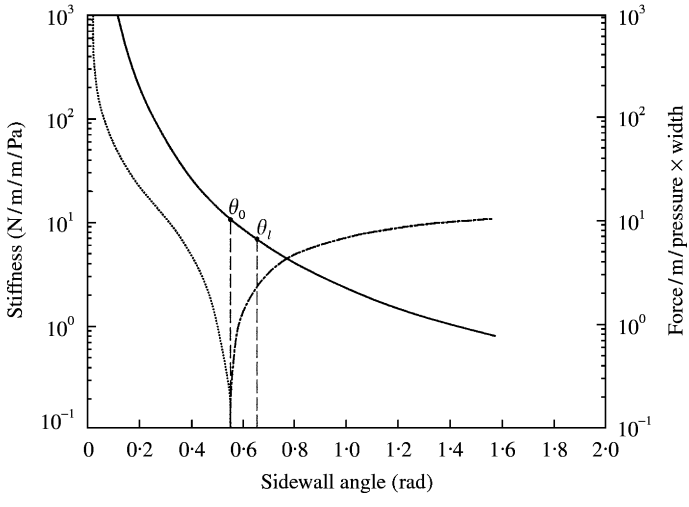

Figure 5. Sidewall stiffness and static load as a function of angle θ. ——, normalized sidewall stiffness; ....., normalized force; F/Pb (tension); ·–·–·–, normalized force (compression).

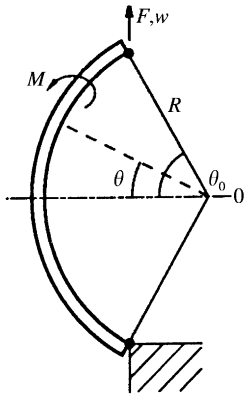

Figure 6. Bending of a pinned sidewall.

At the equilibum position for an unloaded sidewall a zero external force F/Pb is seen in Figure 5 at angle θ_0. The stiffness K_T at this point is given as approximately

$$K_T = \frac{3P}{2}\left(\frac{b}{l_s}\right)^3, \tag{20}$$

showing the cubic dependence of sidewall stiffness upon the aspect ratio. If now the tyre was loaded in compression due to gravity, a force $-F$ is applied and the new equilibrium angle θ_1 is given from equation (19) and shown in Figure 5, which is accompanied by a decrease in sidewall stiffness. To the contrary, when the tyre rotates, a positive centrifugal force F is applied which would give a decreasing sidewall angle and associated increase in sidewall stiffness. These equations could then be used to obtain an estimate for stiffness under any normal loading conditions. The maximum load bearing occurs when $\theta = \pi/2$, while the stiffness at this point takes a minimum of

$$K_T = \frac{P\pi}{4}. \tag{21}$$

2.4. THE BENDING STIFFNESS OF THE TYRE SIDEWALL

Equation (17) gives the stiffness of the one sidewall due to in plane tension. If the sidewall also has a bending stiffness B_s the additional contribution due to bending alone can be simply summed provided that the same deformation pattern is assumed.

The system is shown in Figure 6, a circular arc at length l_s and radius R is stretched by a force F. The terminations are assumed to be pinned as this is the simplest case which will describe the bending behaviour. The lower point is fixed while the upper point moves a small distance w.

The bending moment M at any angle θ is

$$M = FR(\cos\theta - \cos\theta_0) \tag{22}$$

The complementary strain energy C is

$$C = \int_{-\theta_0}^{\theta_0} \frac{M^2}{2B_s} R\,\mathrm{d}\theta. \tag{23}$$

The deflection w due to force F, is given from the principle of minimum total complementary potential energy as

$$w = \frac{\mathrm{d}C}{\mathrm{d}F}$$

or

$$w = \frac{R}{B_s}\int_{-\theta_0}^{\theta_0} M\,\frac{\mathrm{d}M}{\mathrm{d}F}\,\mathrm{d}\theta. \tag{24}$$

Substitution of equation (22) and performance of the integral gives the stiffness $K_b = F/w$

$$K_b = \frac{16B_s}{l_s^3}\,\frac{\theta_0^3}{(4\theta_0 + 2\theta_0\cos 2\theta_0 - 3\sin 2\theta_0)}. \tag{25}$$

Making use of the small angle approximation in equation (7) valid for $0 < \theta < \pi/2$,

$$K_b \approx \frac{32B_s}{\theta_0^2 l_s^3}. \tag{26}$$

The stiffness due to bending therefore also decreases with the aspect angle θ_0, as did the stiffness due to tension.

The total dynamic stiffness K_s can now be written using the small angle approximation and by summing the bending and tension stiffness with the dynamic contribution in equation (10), i.e.,

$$K_s = \frac{32B_s}{l_s^3\theta_0^2} + \frac{P}{4\theta_0^3}(6 + 3\theta_0^2 - \theta_0^4) - \frac{3w^2 m_s}{\theta_0^2}\,\frac{(6 - 5\theta_0^2 + \theta_0^4)}{(6 - \theta_0^2)} - \omega^2 m_s. \tag{27}$$

This expression is plotted in Figure 7 below the ring frequency f_r of the sidewall, which occurs when

$$f_r = \frac{1}{2\pi R}\sqrt{\frac{E_s}{\rho_s}} = \frac{\theta_0}{\pi l_s}\sqrt{\frac{E_s}{\rho_s}}, \tag{28}$$

for which the parameters chosen in Table 1 in reference [1] is around 400 Hz. The static theory is only valid below this point, which can be seen as a slight kink on the curves in Figure 7. The ring frequency will also represent the limit to the simple bulging motion of the sidewall described in Figure 1(a), as was observed in reference [3]. The major dip is associated with the sidewall resonance. The stiffness is proportional to the pressure. Only at low pressures does the sidewall bending become significant. The bending, however, plays a major role in providing some additional damping to the low value associated with the pure tension-controlled behaviour. Figure 8 shows the effect, below the ring frequency, of changing the aspect ratio l_s/b. The stiffness increases roughly in accordance with the cube of b/l_s. A tyre with a short sidewall will therefore have a small angle θ_0, and hence a high stiffness.

3. SIDEWALL STIFFNESS ABOVE THE RING FREQUENCY

At frequencies greater than the ring frequency the curvature of the sidewall can be neglected, and the out-of-plane and axial deformations regarded separately.

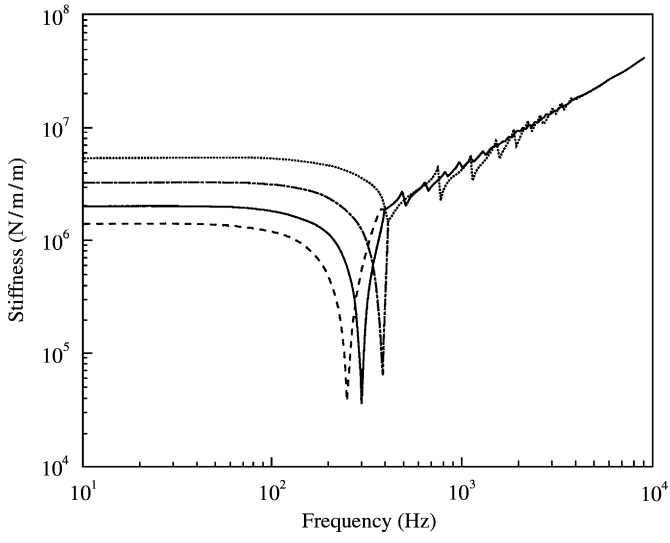

Figure 7. Input sidewall dynamic stiffness as a function of internal pressure, $b = 0{\cdot}2$ m, $l_s = 0{\cdot}08$: ·····, 2 bar; ·–·–, 1 bar; ——, 0·5 bar; - - - -, 0·25 bar.

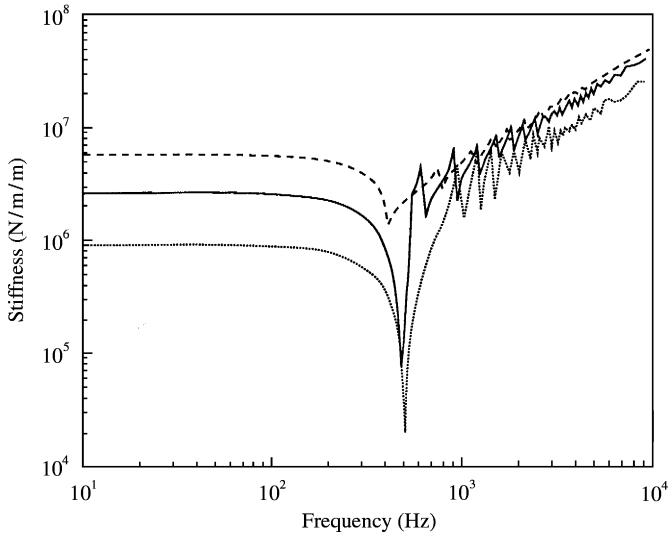

Figure 8. Input sidewall dynamic stiffness as a function of aspect ratio, internal pressure = 2 bar: - - - - - , $l_s = 0{\cdot}08$; $b = 0{\cdot}2$; ——, $l_s = 0{\cdot}08$, b = 0·15; ···, $l_s = 0{\cdot}08$, $b = 0{\cdot}1$.

Assuming pinned joints at either end, the displacement w and force F impose shear force Q_1, and in-plane forces N_1, at the input, as seen in Figure 9:

$$F = Q_1 \sin\theta + N_1 \cos\theta. \tag{29}$$

The displacement at the top is a sum of the radial and axial components:

$$w = w_s \sin\theta + u \cos\theta. \tag{30}$$

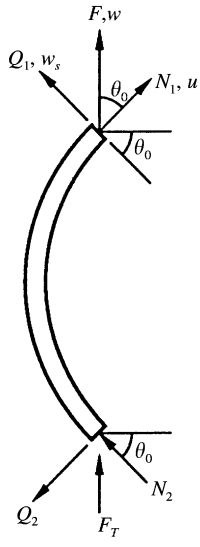

Figure 9. In-plane and shear forces on the sidewall.

The displacement is zero at the base:

$$0 = w_s \cos\theta - u \sin\theta. \tag{31}$$

The transmitted force to the base is

$$F_T = -Q_2 \sin\theta + N_2 \cos\theta, \tag{32}$$

where for zero motion at the base, the related stiffnesses are

$$Q_1 = K_Q w_s, \quad Q_2 = K_{QT} w_s.$$

$$N_1 = K_N u, \quad N_2 = K_{NT} u \tag{33}$$

K_Q and K_{QT} are the input and transfer dynamic stiffness of a straight beam under shear, given in Figure 10. K_N and K_{NT} are likewise the input and transfer dynamic stiffness due to in-plane forces.

Combining equations (29–33) gives the input and transfer stiffness as

$$\frac{F}{w} = K_Q \sin^2\theta + K_N \cos^2\theta, \tag{34}$$

$$\frac{F_T}{w} = -K_{QT} \sin^2\theta_0 + K_{NT} \cos^2\theta_0. \tag{35}$$

3.1. LONGITUDINAL MOTION

For pure axial excitation the impedances are given in reference [9] as

$$Z_N = Z_a \frac{1+\alpha}{1-\alpha}, \quad Z_{NT} = -Z_a \frac{2\alpha^{1/2}}{1-\alpha}, \tag{36}$$

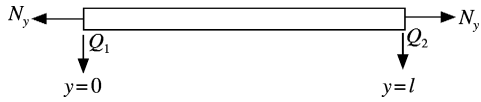

Figure 10. Straightened sidewall subject to tension and bending.

where the characteristic impedance is

$$Z_a = t_s \sqrt{E_s \rho_s},$$

and the attenuation and phase change as a wave travelling $2l$ is

$$\alpha = \exp(-\mathrm{i}2k_L l_s),$$

the longitudinal wavenumber $k_L = \omega(\rho_s/E_s)^{1/2}$ and E_s, ρ_s, t_s are the sidewall longitudinal modulus, density and thickness.

3.2. OUT-OF-PLANE MOTION

The out-of-plane impedances Z_Q and Z_{QT} are controlled by both tension and bending and may be calculated from the straightened version of the sidewall shown in Figure 10.

The wave equation is obtained from equation (8) in reference [1], by setting an infinite shear stiffness and neglecting the rotary inertia ρI_x. The subscripts x are replaced by y,

$$-\frac{\partial^4 w}{\partial y^4} + \chi_y \frac{\partial^2 w}{\partial y^2} + k_{by}^4 w = 0 \tag{37}$$

where

$$\chi_y = N_y/B_s,\ k_{by}^4 = \omega^2 \frac{\mu_s}{B_s}. \tag{38}$$

The mass/area of the belt is μ_s, and B_s is the bending stiffness/unit width. By substituting a travelling wave solution of the form $we^{-\mathrm{i}ky}$, equation (37) becomes

$$k^4 + \chi_y k^2 - k_{by}^4 = 0. \tag{39}$$

The solutions are

$$k_1^2, k_2^2 = -\frac{\chi_y}{2} \pm \sqrt{\frac{\chi_y^2}{4} + k_{by}^4}. \tag{40}$$

When the tension forces dominate $\chi_y^2 \gg 4k_{by}^4$, the wavenumbers are the travelling wavenumber, k_1, and evanescent wavenumber, k_2, which are both tension controlled, seen for example in Figure 11 in the low-frequency regime.

$$k_1 = k_{ty} = \omega\left(\frac{\mu_s}{N_y}\right)^{1/2}, \quad k_2 = -\mathrm{i}(\chi_y)^{1/2}. \tag{41a, b}$$

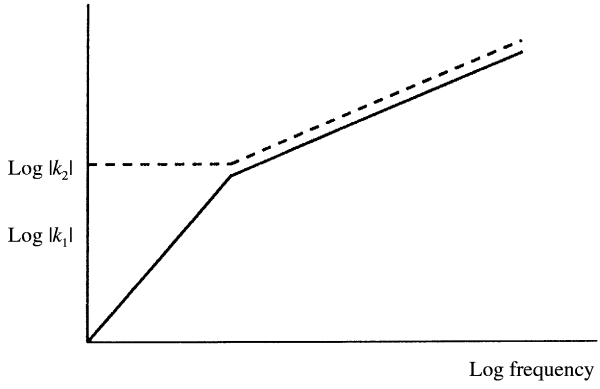

Figure 11. Sidewall wavenumbers due to bending and tension.

Alternatively, when bending forces dominate at high frequencies the usual bending wave numbers occur.

$$k_1 = k_{by} = \omega^{1/2}\left(\frac{\mu_s}{B_y}\right)^{1/4}, \quad k_2 = -\mathrm{i}k_{by} \tag{42a, b}$$

These are shown in Figure 11 in the high-frequency regime.

The real component, k_1, associated with travelling waves can be described approximately as

$$k_1^2 = \frac{k_{ty}^2 k_{by}^2}{(k_{ty}^2 + k_{by}^2)} \tag{43a}$$

and the imaginary component associated with evanescent waves as

$$k_2^2 = -\frac{\chi_y k_{by}^2}{(\chi_y + k_{by}^2)}. \tag{43b}$$

If now the displacement, w, at any point along the beam is represented as a summation of travelling waves and the evanescent waves emanating from $y = 0$,

$$w = A\mathrm{e}^{-\mathrm{i}k_1 y} + r\alpha A\mathrm{e}^{-\mathrm{i}k_1 y} + B\mathrm{e}^{-k_e y}, \tag{44}$$

where $k_e = |k_2|$ and $\alpha = \mathrm{e}^{-2\mathrm{i}k_1 l_s}$ is the attenuation and change in phase of a wave travelling $2l_s$.

A, B are constants. For the pinned support, the reflection coefficient $r = -1$, permitting equation (44) to be reduced to

$$w = A(\mathrm{e}^{-\mathrm{i}k_1 y} - \alpha\mathrm{e}^{\mathrm{i}k_1 y}) + B\mathrm{e}^{-k_e y}. \tag{45}$$

As the bending moment is zero at $y = 0$,

$$0 = -B_s \left.\frac{\partial^2 w}{\partial y^2}\right|_{y=0}, \tag{46}$$

giving the ratio between constants as

$$\frac{B}{A} = \left(\frac{k_1}{k_e}\right)^2 (1 - \alpha). \tag{47}$$

The out-of-plane force F is given in equation (27) in reference [1] as

$$F = \left(Q + N_y \frac{\mathrm{d}w}{\mathrm{d}y}\right)\bigg|_{y=0} \tag{48}$$

The shear force Q is

$$Q = -B_s \frac{\partial^3 w}{\partial y^3}. \tag{49}$$

Equations (45–49) yield the input dynamic stiffness K_Q

$$K_Q = B_s k_1 k_e \left\{\frac{\mathrm{i}k_e(1 + \alpha)(k_1^2 + \chi_y)}{(k_e^2 + k_1^2)(1 - \alpha)} - \frac{k_1(k_e^2 + \chi)}{(k_e^2 + k_1^2)}\right\}. \tag{50}$$

The transfer dynamic stiffness is found by setting $y = 1$ in equation (48)

$$F(1) = B_s A[\mathrm{i}k_1(\mathrm{e}^{-\mathrm{i}k_1 l_s} + \alpha \mathrm{e}^{\mathrm{i}k_1 l})(k_1^2 + \chi_y)] \tag{51}$$

and the displacement in equation (45) at $y = 0$,

$$w(0) = A\left(1 - \alpha + \frac{B}{A}\right). \tag{52}$$

Equations (47), (51) and (52) yield the transfer dynamic stiffness K_{QT},

$$K_{QT} = -2B_s \frac{\mathrm{i}k_1 k_e^2 \mathrm{e}^{-\mathrm{i}k_1 l_s}(k_1^2 + \chi_y)}{(1 - \alpha)(k_e^2 + k_1^2)}. \tag{53}$$

The expressions for input and transfer dynamic stiffness take two extremes. When tension dominates, $k_t < k_b$, $k_e \gg k_t$, $k_1 = k_t$

$$K_Q = \frac{\mathrm{i}\omega^2 \mu_s}{k_t} \frac{1 + \alpha}{1 - \alpha}, \quad K_{QT} = \frac{-\mathrm{i}\omega^2 \mu_s}{k_t} \frac{2\alpha^{1/2}}{1 - \alpha}. \tag{54}$$

At higher frequencies, bending dominates and $k_b > k_t, k_e = k_b, k_1 = k_b$.

$$K_Q = \frac{\mathrm{i}\omega^2 \mu_s}{k_b}\left(\frac{1 + \alpha}{1 - \alpha} + \mathrm{i}\right), \quad K_{QT} = \frac{-\mathrm{i}\omega^2 \mu_s}{k_b} \frac{2\alpha^{1/2}}{1 - \alpha}. \tag{55}$$

The change in regime between tension and bending occurs when $k_t = k_b$ or when

$$\omega = \frac{N_y}{\sqrt{B_s \mu_s}}, \quad N_y = \frac{P l_s}{2\theta_0}. \tag{56}$$

For a Young's modulus of $E_s = 3 \times 10^7\ \mathrm{N/m^2}$ and pressure 2 bar, for the unloaded tyre there is a change in regime at 1300 Hz. The implication is that for most practical purposes the sidewall bending can be neglected, as the observation is that interior vehicle noise only

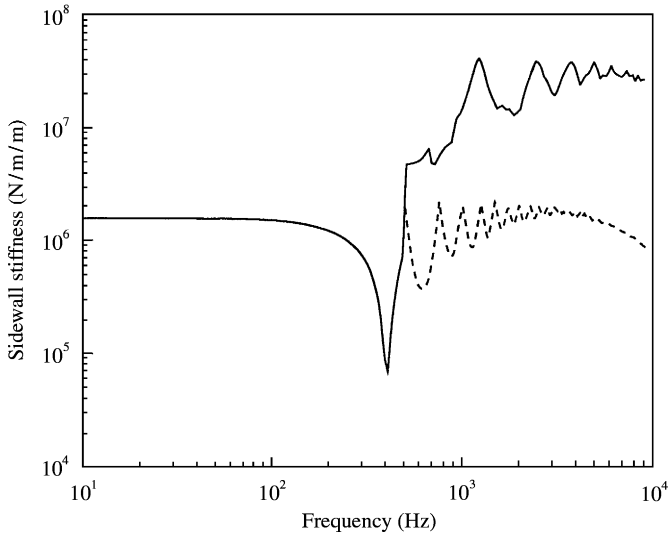

Figure 12. Transfer dynamic stiffness, $P = 2$ bar. $l_s = 0{\cdot}1$ m, $b = 0{\cdot}16$ m, $E_s = 6{\cdot}7 \times 10^7$, $t = 7 \times 10^{-3}$, uniform loading $k_x = 0$: ——, longitudinal contribution; - - - -, tension contribution.

tends to be influenced by hub transmission at frequencies less than 1000 Hz [10]. The input dynamic stiffness K_s of the sidewall above the ring frequency is therefore obtained from equations (34), (36) and (54).

$$K_s = \mathrm{i}\omega^2 \varsigma_s \left[\left(\frac{1 + \alpha_t}{1 - \alpha_t} \right) \frac{\sin^2 \theta_0}{k_t} + \left(\frac{1 + \alpha_L}{1 - \alpha_L} \right) \frac{\cos^2 \theta_0}{k_L} \right], \tag{57}$$

where $\alpha_t = \mathrm{e}^{-2\mathrm{i}k_t l_s}$, $\alpha_L = \mathrm{e}^{-2\mathrm{i}k_L l_s}$.

The transfer dynamic stiffness K_T is given from equations (35), (36) and (55)

$$K_T = 2\mathrm{i}\omega^2 \varsigma_s \left[\frac{\alpha_t^{1/2}}{(1 - \alpha_t)} \frac{\sin^2 \theta_0}{k_t} - \frac{\alpha_L^{1/2}}{(1 - \alpha_L)} \frac{\cos^2 \theta_0}{k_L} \right], \quad \omega > \frac{c_L}{k}. \tag{58}$$

These two components seen above the ring frequency at 500 Hz are plotted in Figure 12. The longitudinal wave component is about an order of magnitude greater than the pressure wave component.

The underlying assumption in this analysis is that the waves radiate normally from the input line of the belt, which means that the upper curve in Figure 12 would be appropriate for the transmission of vibration in the region of the contact patch. However, when a wave is travelling in the free belt with a non-zero wavenumber k_x, there is radiation into the sidewall at angles determined by the relative wavenumbers of the belt k_x and sidewall k in accordance with the vector diagram in Figure 13.

The true normal wavenumber k', is given by

$$k' = \sqrt{k^2 - k_x^2}, \tag{59}$$

where k is either k_t or k_L, for tension or longitudinal waves. The tension wave speed given from equation (56) is

$$c_T = \sqrt{\frac{Pl_s}{2\theta_0 \mu_s}}$$

is about 50 m/s which is slower than the wave in the belt.

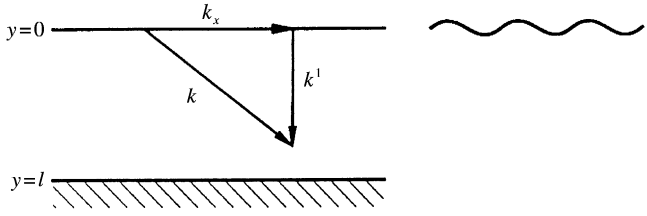

Figure 13. Wavenumber vectors in the sidewall.

Thus the normal wavenumber k_t' vector is reduced to

$$k_t' = (k_t^2 - k_x^2)^{1/2}. \tag{60}$$

The longitudinal wave speed in the sidewall is, however, about 150 m/s, greater than the out-of-plane belt wave, which is expected from reference [1] to be about 100 m/s. The wavenumber k_L' is therefore likely to be evanescent, taking the form,

$$k_L' = -\mathrm{i}k_e = -\mathrm{i}(k_x^2 - k_L^2)^{1/2}. \tag{61}$$

The input sidewall stiffness K_s, shown in equation (57) then becomes for $k_L < k_x$

$$K_s = \frac{\mathrm{i}\omega^2\mu_s}{k_t'}\left(\frac{1+\alpha_t}{1-\alpha_t}\right)\sin^2\theta_0 - \frac{\omega_2\mu_s}{k_e}\left(\frac{1+\alpha_L}{1-\alpha_L}\right)\cos^2\theta_0, \tag{62}$$

where $\alpha_t = \mathrm{e}^{-2\mathrm{i}k_t' l_s}$, $\alpha_L = \exp(-2k_e l_s)$, and the transfer stiffness K_T is

$$K_T = -2\omega^2\varsigma_s\left[\frac{\mathrm{i}\alpha_t^{1/2}}{(1-\alpha_t)}\frac{\sin^2\theta_0}{k_t} + \left(\frac{\alpha_L^{1/2}\cos^2\theta_0}{1-\alpha_L k_e}\right)\right]. \tag{63}$$

The tension wavespeed is increased but the transmission still takes the same form as Figure 12. However, the transmission from the longitudinal wave almost vanishes, while at input line with the belt the evanescent longitudinal wave gives a mass loading term, calculated from equation (62) as approximately μ_s/k_x. This is the straight line trend seen in Figures 7, 8 and 14 above the ring frequency at about 500 Hz. In Figure 7 it is shown that the input dynamic stiffness is independent of pressure. In Figure 14 the input and transfer dynamic stiffness are compared for a belt wave speed at 100 m/s. The transfer dynamic stiffness is only controlled by the tension wave, as the evanescent longitudinal wave causing the mass loading at the input is greatly attenuated at the hub when $y = 1$. The resonances seen in Figure 14 are also associated with the tension wave. Figure 15 shows the effect of the aspect ratio in transmitted force. The broad belt is stiffer below the ring frequency, as discussed in section 2 but transmits less force above the ring frequency because of the smaller equilibrium angle θ_0.

4. THE INPUT MOBILITY OF THE BELT

In reference [1] the wave equations, input mobilities and transfer mobilities of a belt with a sidewall were calculated in general terms and displayed for a sidewall of zero stiffness. Now that the sidewall stiffness K_s is available from equations (27) and (62), the same quantities can be recomputed for the forcing arrangement displayed in Figure 16 where a line force distribution $F\cos m\,\pi y/b$ acts at $x = 0$ along the belt.

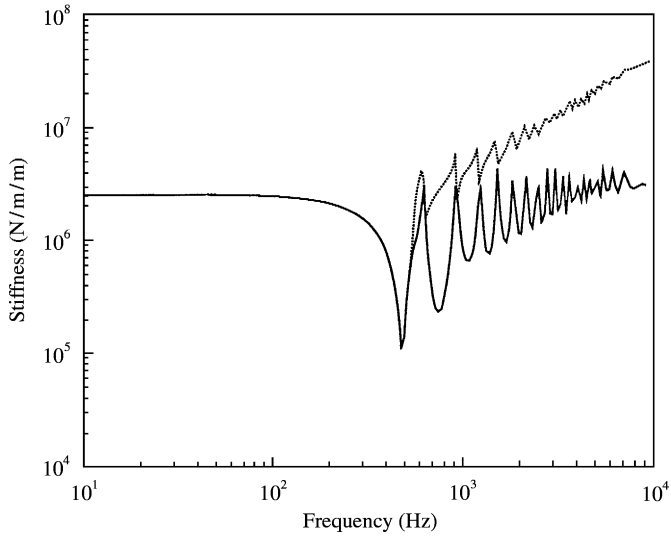

Figure 14. Modulus of input and transfer dynamic stiffness for $l_s = 0{\cdot}08$, $b = 0{\cdot}16$, $P = 2$ bar, belt wavespeed $cx = 100$ m/s: ——, transfer; ·····, input.

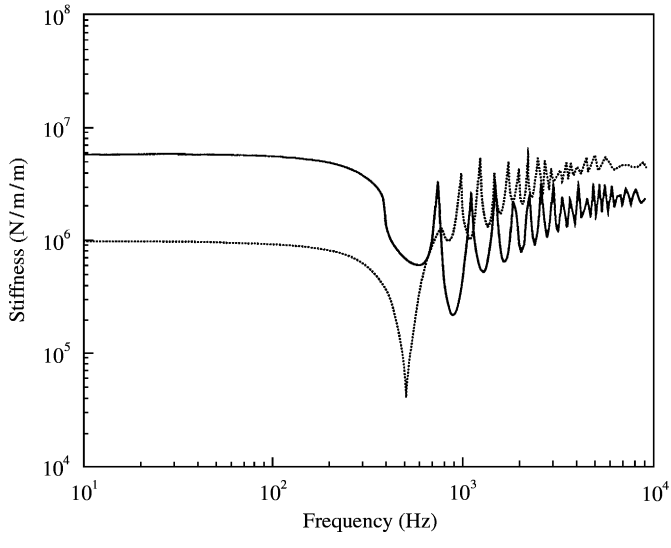

Figure 15. Transfer dynamic stiffness as a function of aspect ratio for the pressure $P = 2$ bar, belt wavespeed $cx = 100$ m/s, $l_s = 0{\cdot}08$ m: ——, $b = 0{\cdot}2$; ·····, $b = 0{\cdot}1$.

The same belt parameters are used in reference [1], and displayed in Table 1 in reference [1]. The dispersion relations for the real roots only for cross belt mode orders $m = 0$, 2, 4, 6 are displayed in Figure 17. If a comparison is made with Figure 9 in reference [1] it can be seen that the sidewall only significantly affects the $m = 0$ wave below the travelling wave cut on at about 150 Hz. At lower frequencies the sidewall stiffness acts as a Winkler foundation, or a set of uniform springs of stiffness 2 K_s/m, permitting no wave motion in the belt until a frequency of

$$f = \frac{1}{2\pi}\sqrt{\frac{2K_s}{b\mu_s}}, \tag{64}$$

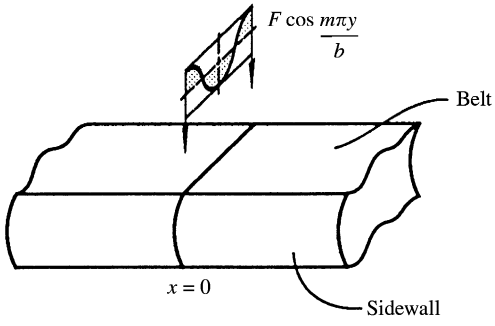

Figure 16. Line excitation of an infinite belt with sidewalls.

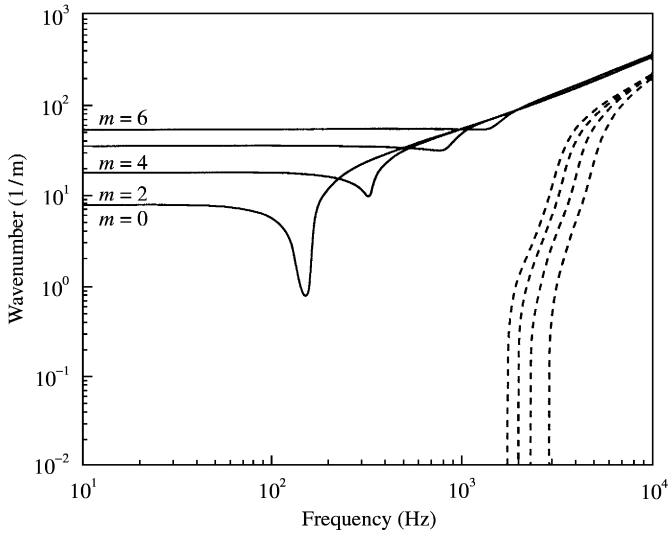

Figure 17. Real parts of the roots for wavenumbers for a tensioned tyre with sidewalls, $m = 0, 2, 4, 6$: ——, root 1; - - - - -, root 2.

when the belt mass has its fundamental resonance with the sidewall stiffness. The stiffness below this frequency seen by a uniform line force on the belt is indicated by the horizontal line of the dispersion relationships. The input mobilities defined by equations (47–49) in reference [1] are shown in Figure 18 for the same propagating modes. The $m = 0$ mode corresponds to the mobility of a line excited belt. An infinite sum of the modal responses would give the mobility of a point excited belt. The belt sidewall resonance at 130 Hz is the lowest that can occur below which there is no propagation of energy along the belt. The cut on frequencies of the $m = 2$, 4, 6 bending waves are seen between 300 Hz and 1·6 Hz. These are almost unchanged from Figure 10 of reference [1]. The cut on of the $m = 0$, 2, 4, 6 "rotational waves" are also seen between 3 and 5 kHz as before. These "rotational waves" are described in reference [1] as a degenerate flexural wave with rotation about the neutral axis but there are only in-plane rather than out-of-plane displacements.

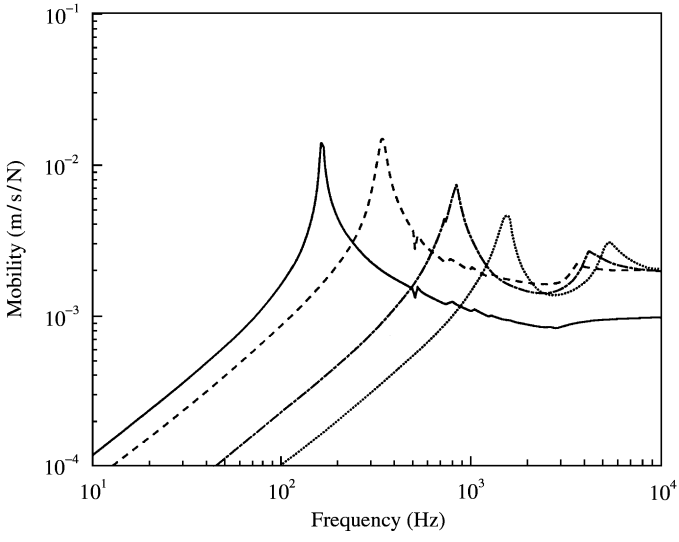

Figure 18. Input mobilities for a line excited infinite tensioned belt with sidewalls. ——, $m = 0$; - - - -, $m = 2$; –·–·, $m = 4$; ·····, $m = 6$.

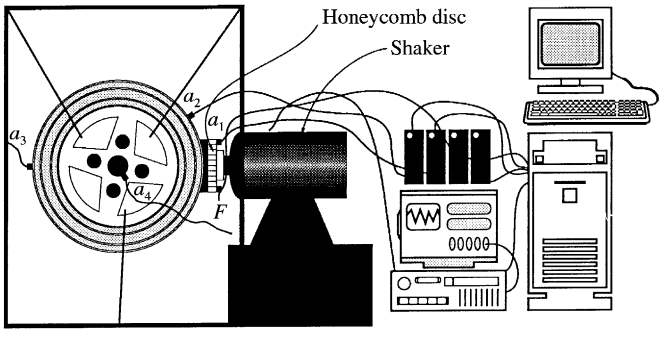

Figure 19. Tyre test arrangement.

5. EXPERIMENTAL MEASUREMENTS FOR THE $m = 0$ MODE FOR INPUT MOBILITY, BELT ATTENUATION, AND FORCE TRANSMISSION TO THE HUB

An attempt was made to support the modelling with some experimental measurements. A tyre was mounted on a lightweight aluminum hub which has an additional central mass of 30 kg. This was suspended with rubber rope in the arrangement shown in Figure 19. The shaker was attached to a honeycomb aluminium pad of 0·15 m diameter. The honeycomb pad and the belt with immediate contact weighed 0·66 kg. Accelerometers were attached at positions $a1$, $a2$, $a3$ and $a4$ to monitor the input accelerance, attenuation around the belt and the force transmitted to the hub. A Kistler force gauge was interposed between the pad and shaker. For most tests a 2 bar air pressure was used.

5.1. INPUT ACCELERANCE AND ATTENUATION AROUND THE BELT

The input accelerance modulus of the tyre was measured and is shown in Figure 20. The fundamental resonance of the belt upon the local sidewall stiffness occurred at about

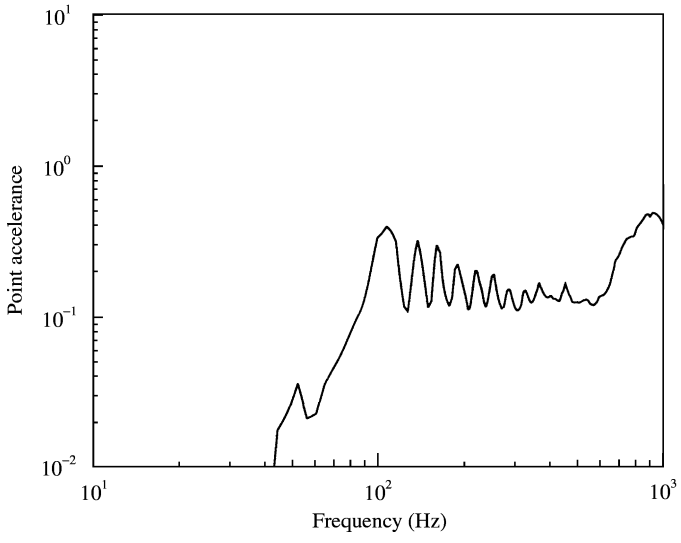

Figure 20. Input accelerance modulus of the tyre.

110 Hz. The local stiffness beneath the pad is measured as $3{\cdot}16 \times 10^5$ N/m from the slope at the low-frequency accelerance. The low-frequency prediction of the stiffness below a pad is given from Figure 12 as $1{\cdot}5 \times 10^6$ N/m/m. The sidewall stiffness/length is quoted [4] for a similar tyre to be $1{\cdot}93 \times \times 10^6$ N/m/m. This predicted value is multiplied by twice the pad diameter to account for both sidewalls and gives $4{\cdot}5 \times 10^5$ N/m, which is a reasonable estimate of the measured value, giving strong support for the theory for static stiffness. The accelerance above 100 Hz displays resonances associated with waves propagating around the belt, which have completely disappeared by 500 Hz due to the high damping. A modal model would no longer be appropriate above this frequency.

The mean value of the point accelerence is unfortunately dominated by the pad mass, giving a lower value than would be expected from Figure 18. The attenuation around the belt is $a3/a2$ as displayed in Figure 21. At 10 Hz, there is no attenuation because of rigid body motion. The bending waves cut on at about 110 Hz and some resonances associated with modes around the belt are seen until 400 Hz. The attenuation due to damping is clear above this frequency. The sharp peak at 400 Hz has low damping and is therefore likely to be related either to a resonance of the hub, or the belt ring frequency. This peak is also seen in Figure 22.

5.2. THE EFFECT OF TYRE PRESSURE OF TRANSMISSION AROUND THE BELT AND FORCE TRANSMITTED TO THE HUB

The acceleration $a3/a2$ between either side of the belt is displayed in Figure 22 for 0, 1, 1·5, 3 bar. The ratio is unity at low frequencies until the "wheel hop" frequency around 20 Hz when the wheel bounces on the contact patch. The sidewall stiffness is shown to be strongly pressure-dependent. The lowest belt mode cuts on at the belt/sidewall resonance at 80 Hz for the 0 bar tyre and 120 Hz for the 3 bar tyre. Above this frequency the transmission around the belt increases with increasing pressure because of the belt wavespeeds.

Comparative theoretical attenuation for pressures 0, 1, 2, 3 bar is displayed in Figure 23. The theoretical tyre is of infinite length and so there is no low-frequency transmission for

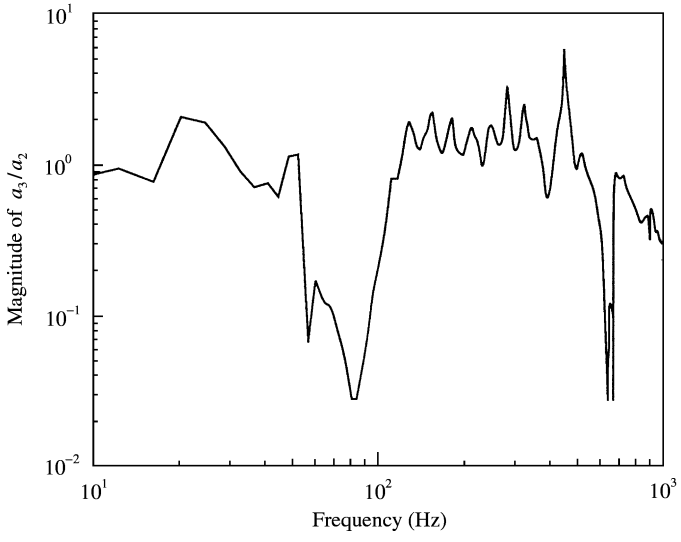

Figure 21. Attenuation of vibration around the belt $a3/a2$, pressure = 2 bar.

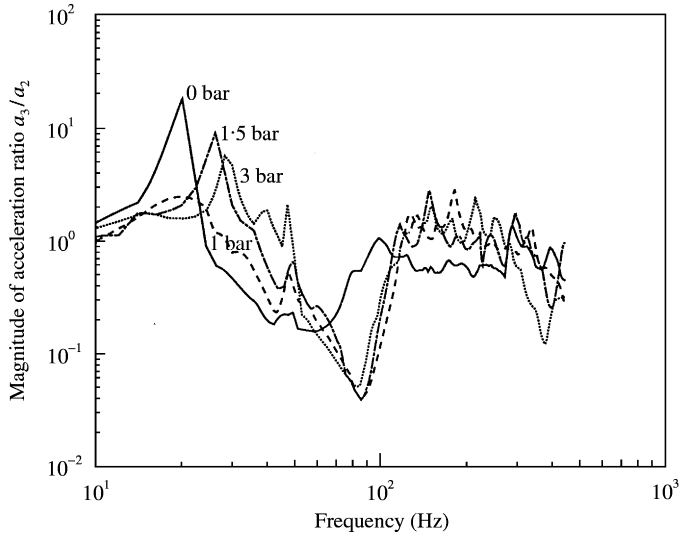

Figure 22. Attenuation of vibration around the belt $a3/a2$, pressure = 0, 1, 1·5, 3 bar.

rigid body motion. Transmission only begins above the belt sidewall resonance, at 60 Hz for 0 bar and 150 Hz for 3 bar. These are in the correct range although a larger range than the measurement is displayed. The 0 bar measurement depends only on the sidewall bending terms selected which is rather low because a pinned–pinned sidewall value was assumed in the theory rather than a more practical pinned–clamped value. At higher frequencies the attenuation decreases with increasing pressure as was the trend with the measurements, in Figure 22. The dips noted around 500 and 700 Hz correspond to sidewall resonances acting as a vibration absorber. There are, of course, no belt resonances in Figure 23 as in Figure 22 because the belt is of infinite extent.

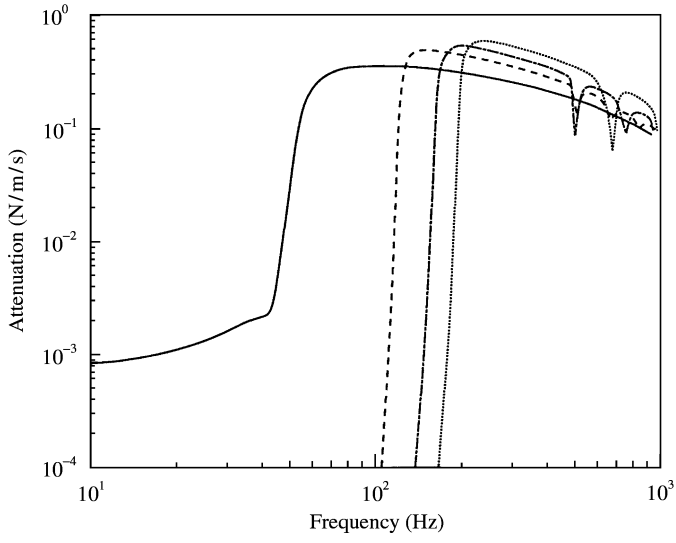

Figure 23. Theoretical attenuation around the belt $a3/a2$, pressure = 0, 1, 2, 3 bar.

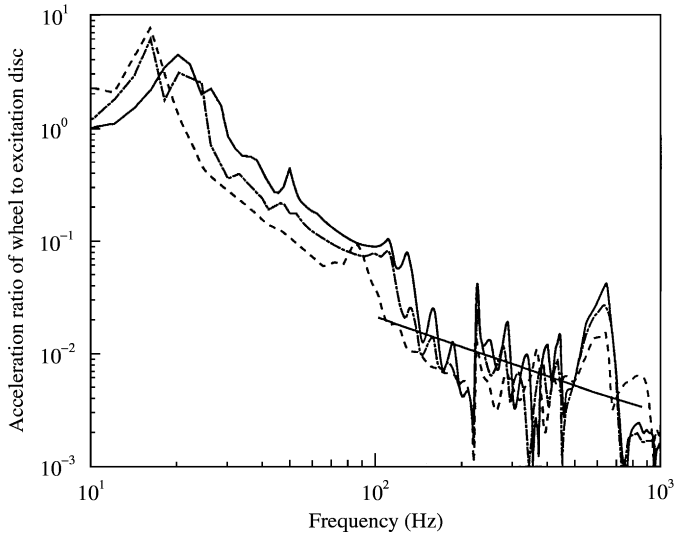

Figure 24. Acceleration ratio from the belt input to the hub $a4/a1$, pressure = 0, 1, 2 bar.

The ratio of measured hub acceleration to input pad acceleration is plotted in Figure 24. The dynamic stiffness of the sidewall beneath the pad is $2bK_T$, i.e.,

$$2bK_T = \frac{F_T}{w_1}, \tag{65}$$

where b is the diameter of the pad. The transfer apparent mass is $2bK_T/\omega^2$. From the experimental measurements the ratio of the pad and hub acceleration is

$$\frac{a_4}{a_1} = \frac{K_T}{K_s - \omega^2 M}, \tag{66}$$

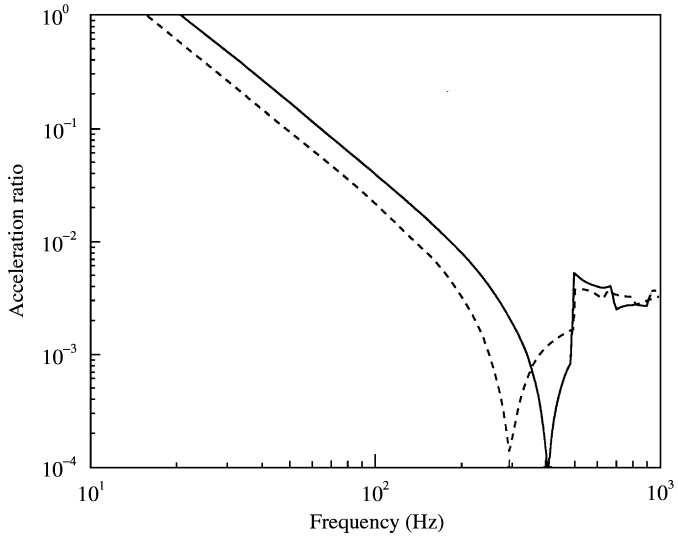

Figure 25. Theoretical acceleration ratio from the belt input to the hub, pressure = 0, 2 bar.

where M is the hub mass of 30 kg. The wheel hop resonance, when transmission to the hub is greatest, occurs when $K_s = \omega^2 M$, seen between 15 and 30 Hz in Figure 24. The transmission is then stiffness-controlled until the belt/sidewall resonances around 100 Hz when another peak in transmission occurs. There is then a period of some interference dips when resonances occur around the belt. The sharp resonant feature at about 220 Hz is independent of pressure and so probably corresponds to the resonance within the air cavity when the circumference of the tyre is equal to one acoustic wavelength. The large pressure dependent peak at 600 Hz is probably associated with a resonance of the hub, seen also in Figure 22. These trends were modelled using the expressions in equations (64) and (65) and the upper curve of Figure 12. The wheel hop resonance and the belt sidewall resonance are included but the stiffness controlled region in Figure 24 until 300 Hz is quite well modelled by the curves in Figure 25. The high-frequency values are also in the correct region.

6. CONCLUSIONS

A sidewall model has been developed for a low-frequency and also for the high-frequency regions on either side of the sidewall ring frequency. The stiffness at low frequency is controlled by the sidewall/belt aspect ratio and the pressure. The high-frequency model will be limited when the first mode cuts in across the sidewall thickness.

At high frequencies, the stiffness depends upon the belt wave speed. Below the contact patch the imposed motion is in phase, and the transmission through the sidewall to the hub is dominated by the sidewall longitudinal waves. However, for the unloaded belt elsewhere the wave speed of the belt is such that the sidewall transfer stiffness becomes much less than in the contact patch. The longitudinal wave in the sidewall becomes evanescent, not transmitting effectively and so the tension wave in the sidewall becomes dominant, at least until 1 kHz when bending becomes a major factor.

These suggestions from the theoretical work were supported by some experimental measurements, which were unfortunately only reliable below about 600 Hz. However, the good agreement below this point indicates that the sidewall in the vicinity of the contact

patch is responsible for most transmission to the hub, rather than the radiation to the sidewall from waves propagating around the belt.

The sidewall only seems to affect belt vibration below the resonance of the belt upon the sidewall at about 100 Hz. Below this frequency, the sidewall stiffness dominates the tyre response, and above this frequency, waves can propagate around the tyre.

REFERENCES

1. R. J. PINNINGTON and A. R. BRISCOE 2002 *Journal of Sound and Vibration* **253**, 969–987. A wave model for a pneumatic tyre belt.
2. W. KROPP 1989 *Applied Acoustic* **20**, 181–192. Structure-borne sound on a smooth tyre.
3. K. SMETS 1995 *M.Sc. Thesis, University of Southampton*. Vibration and wave tyre recognition in automotive tyres.
4. P. W. A. ZEGELAAR. *SAE Paper* 971101. Modal analysis of an automotive tyre in-plane vibration.
5. G. MASTINU, S. GAIAZZI, F. MONTAVANO and D. PIROLA 1997 in *Tyre Models for Vehicle Dynamic Analysis, Proceedings of the second International Colloquium on Tyre Models for Vehicle Dynamic Analysis* (F. Bohm and H-P. Willumeit, editors) 2–21. Lisse, Abingdon: Swets & Zeitlinger. Semi-analytical tyre model for steady-state and transient simulations.
6. L. E. KUNG and W. SOEDEL 1985 *Journal of Sound and Vibration* **102**, 329–346. Natural frequencies and mode shapes of an automotive tyre with interpretation and classification using 3-D computer graphics.
7. R. J. PINNINGTON 1997 *Journal of Sound and Vibration* **204**, 271–289. The axisymmetric wave transmission properties of pressured flexible tubes.
8. R. J. PINNINGTON 1997 *Journal of Sound and Vibration* **204**, 291–310. Axisymmetric wave transfer function of flexible tubes.
9. R. J. PINNINGTON, L. C. CHOW and R. C. N. LEUNG 1995 *Journal of Sound and Vibration* **184**, 299–310. An investigation of an elastic sandwich treatment.
10. Refinement by Design 1996 Road Noise Workshop, Rover Group, Gaydon, 3 April.